Supplementary information

Plasmon-Mediated Highly Enhanced Photocatalytic Degradation of Industrial Textile Effluent Dyes using Hybrid ZnO@Ag Core-shell Nanorods

V.P.Dinesh[a], P.Biji[a*], Anuradha Ashok[a], S.K.Dhara[b], M.Kamaruddin[b], A.K.Tyagi[b] and Baldev Raj[a]

[a] Nanotech Research Facility, PSG Institute of Advanced Studies, Coimbatore - 641 004, INDIA

[b] Indira Gandhi Center for Atomic Research, Kalpakkam - 603102, INDIA

*Corresponding Author Email: bijuja123@yahoo.co.in

1. FE-SEM studies of Hybrid ZnO@Ag core-shell nanorods with EDX

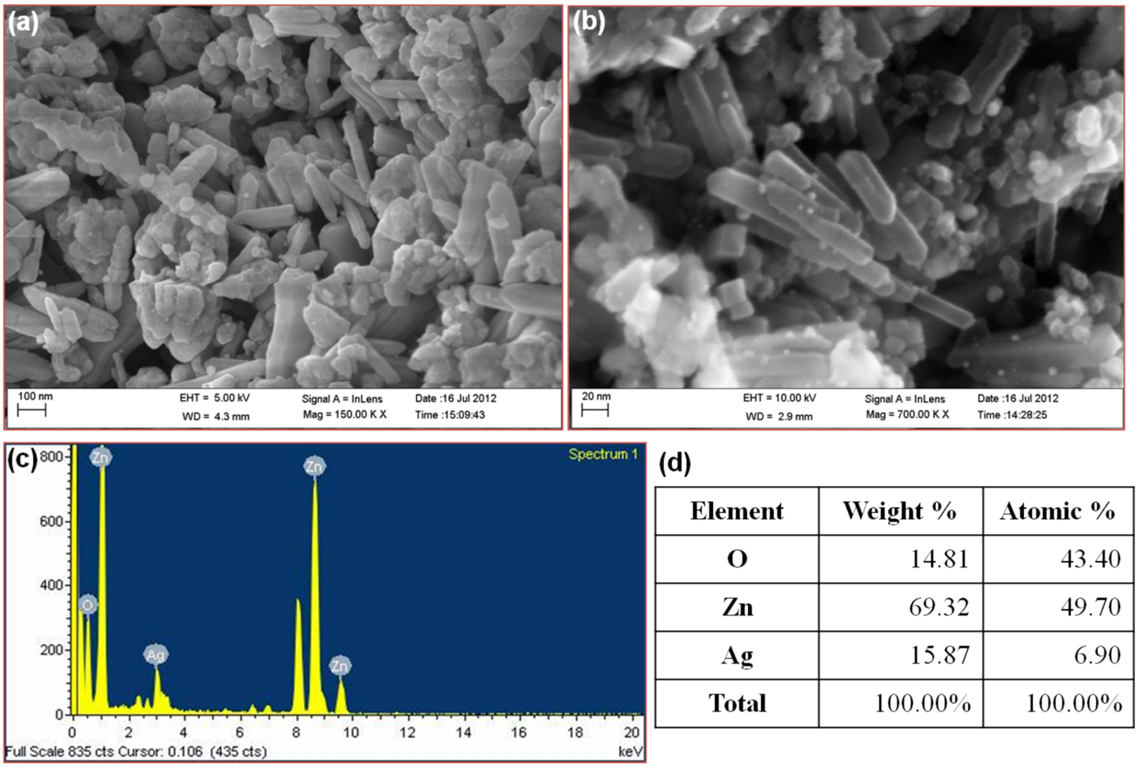

Element	Weight %	Atomic %
O	14.81	43.40
Zn	69.32	49.70
Ag	15.87	6.90
Total	100.00%	100.00%

Figure S1 (a,b) FE-SEM image and (c,d) EDX spectrum of hybrid ZnO@Ag core-shell nanorods

The FE-SEM images clearly show the synthesised hybrid ZnO@Ag core-shell nanorods with different magnifications. It clearly illustrates the mono-dispersed nature of ZnO nanorods with the diameter of around 20 nm (high aspect ratio – 6:1). EDS spectrum (S1c, d) confirms the presence of Ag nanoclusters in the hybrid structures with the loading percentage of 6.90 atomic %.

2. X-Ray Diffraction studies of ZnO nanorods and ZnO@Ag core-shell nanorods

The XRD pattern of ZnO nanorods (Figure S2a) shows its characteristic peaks with hexagonal wurtzite structure with space group of $P6_3mc$ (186) (a. 3.249 and c. 5.206). Our data is in well agreement with the Joint Committee on Powder Diffraction Standards (JCPDS) card no JCPDS PDF no 36-1451 [1]. The strongest peaks observed at 2θ values of 31.79°, 34.421°, 36.252°, 47.51°, 56.602°, 62.862°, 67.961° and 69° corresponding to the lattice planes (100), (002), (101), (110), (103), (112), and (201) respectively. The XRD pattern of Ag modified ZnO nanorods (Figure S2b) shows characteristic peak of Ag at 2θ of 38.11°, 44.27° and 64.42° (JCPDS PDF no. 04-0783) (ASTM., 1999). In both XRD patterns no other impurity peaks are observed for Zn or $Zn(OH)_2$ which clearly signify the purity and the phase structure of ZnO. The strongest peaks observed at 2θ values of 31.79°, 34.421°, 36.252°, 47.51°, 56.602°, 62.862°, 67.961° and 69° corresponding to the lattice planes (100), (002), (101), (110), (103), (112), and (201) respectively.

Optimization of Ag nanoclusters loading onto the ZnO nanorod surfaces was performed by XRD analyses of the core-shell nanorods having varied Ag loading. Hybrid core-shell nanorods were formed through functionalization process. Thus by tuning the concentration of the linker molecules we can change the loading percentage of Ag on the surface of ZnO nanorods. The corresponding XRD patterns showed both Ag peaks and ZnO wurtzite structure. Intensity of Ag peaks at 2θ values of 38.116°, 44.227° and 64.426° are monitored along with their full width half maximum (fwhm). Alteration in the crystallinity of ZnO nanorods is due to the heterostructure formation and difference in the ionic radii of Zn^{2+} and Ag^{+} which are 0.074 nm and 0.126 nm respectively [2]. Ionic radii of Ag^{+} ion is greater than Zn^{2+} ion, and this difference results in the expansion of lattice parameter for hybrid ZnO@Ag core-shell nanorods. Heterogeneous nucleation of hybrid nanorods is obtained in the presence of Ag^{+} ions in the ZnO structure. Thus Ag atoms can be incorporated into the ZnO lattice by substitution process. No shift was observed for ZnO peaks, confirming the suface doping or segregation of Ag nanoclusters on the grain boundaries of ZnO nanorods [3].

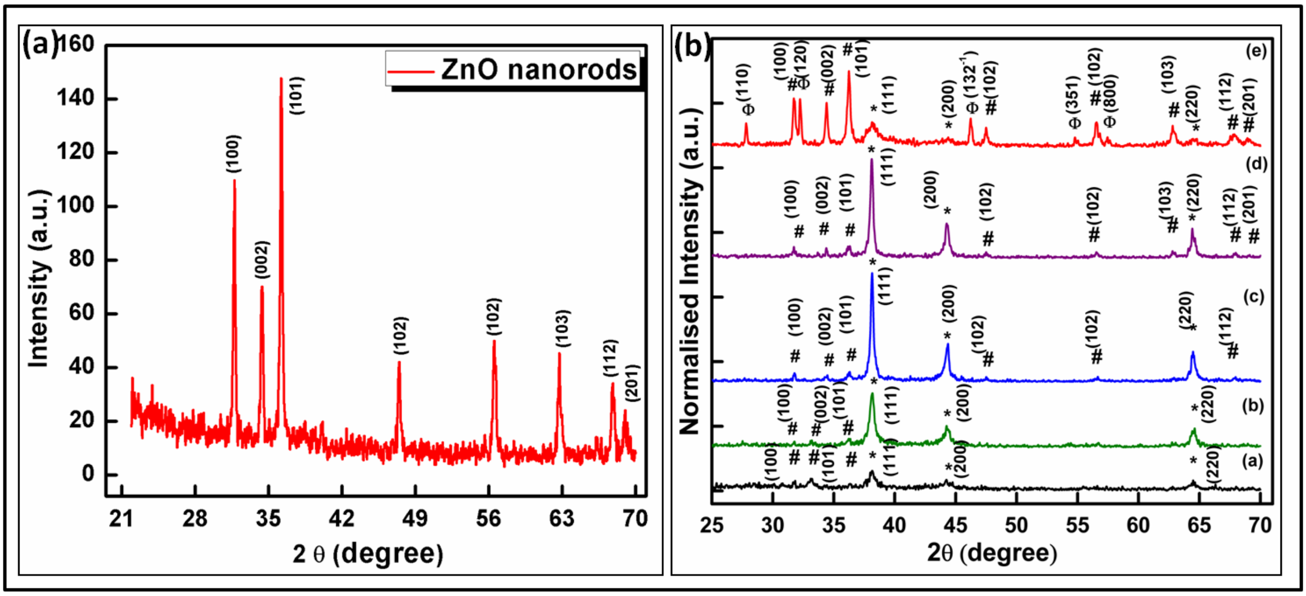

Figure S2 XRD pattern of (a) ZnO nanorods XRD (b) Hybrid ZnO@Ag core-shell nanorods with 1M (i), 1.25M (ii), 1.5M (iii), 1.75M (iv) and 2M (v) concentrations of linker (APTMS) molecules.

Table S1. Parameters obtained for the hybrid ZnO@Ag core-shell nanorods from XRD analysis.

Concentration of Linker (APTMS), (M)	hkl planes	2θ (deg)	*fwhm* (deg)
1	*Ag*		
	(111)	38.116	0.630
	(200)	44.272	0.840
	(220)	64.426	0.993
	ZnO (101)	36.252	2.650
1.25	*Ag*		
	(111)	38.116	0.574
	(200)	44.272	0.646
	(220)	64.426	0.371
	ZnO (101)	36.252	0.218
1.5	*Ag*		
	(111)	38.116	0.396
	(200)	44.272	0.378
	(220)	64.426	0.461
	ZnO (101)	36.252	0.396
1.75	*Ag*		
	(111)	38.116	0.388
	(200)	44.272	0.372

	(220)	64.426	0.491
	ZnO (101)	36.252	0.276
2	*Ag*		
	(111)	38.116	1.058
	(200)	44.272	1.346
	(220)	64.426	0.388
	Ag_2O_3		
	(110)	27.694	0.173
	(120)	32.20	0.210
	$(1\bar{3}2)$	46.251	0.273
	$(2\bar{0}2)$	54.890	0.269
	(220)	57.531	0.214
	ZnO (101)	36.252	0.346

Generally Ag act as an amphoteric dopant in ZnO and substitution of Ag_1* interstitial over the Zn^{2+} sites can be expressed by the following reaction [4];

$$2Ag \longrightarrow Ag_1^* + Ag'_{Zn} \text{ or } (Ag_2O) \longrightarrow Ag_1^* + Ag'_{Zn} + ZnO) \text{-----------------------} \quad (1)$$

Using Bragg’s law we can calculate lattice constants *a* and *c* for wurtzite ZnO nanorods.

$$n\lambda = 2d\sin\theta \quad \text{---} \quad (2)$$

where, *n* is the order of diffraction; λ is the wavelength of X-ray used; and *d* is the spacing between planes of given Miller indices *h*, *k*, and *l*. For the hexagonal structure of ZnO nanorods with (100) orientation at 2θ = 31.79° and for (002) orientation at 2θ = 34.42° the lattice constant were calculated as 3.249 A° (*a*) and 5.206 A° (*b*) respectively. After the incorporation of Ag^+ ions an appreciable change in lattice parameters occurs (3.270 A° and 5.239 A°) due to the difference in their ionic radii. The change in the intensity of ZnO@Ag core-shell nanorods of different concentration demonstrates the loading efficiency of Ag onto the ZnO nanorods (vide Figure S2). Also it is evident from those Ag nanoclusters loading have an effect over the crystallinity of ZnO as indicated by the differences shown in the *fwhm* values. From table S1 we can understand that Ag loading rate changes the *fwhm* values correspondingly, but at higher APMTS concentration (2M) both intensity and *fwhm* differs from the others. Moreover, extra peaks corresponding to Ag_2O_3 (JCPDS PDF no.40-0909) at 2θ values of 27.694°, 46.24°, 54° and 57.4° with respective planes (110), (132), (202) and (220) also were observed. At higher concentration of APTMS linker molecule (2M), Ag clusters tend to get agglomerated and forms larger sized particles. Thus, the drastic increase in concentration of linkers induces aggregation of Ag nanoclusters on the surface of ZnO nanorods. Loading percentage of Ag onto ZnO nanorods was found to be 6.90% atomic percentage for the optimized concentration which is obtained from the EDS spectrum of ZnO@Au core-shell nanorods (Figure S1).

3. Binding energy values from XPS analysis

Table S2. Summary of parameters obtained from XPS analysis on hybrid ZnO@Ag core-shell nanorods.

Element description	Binding energy (eV)	Binding energy (eV) (Standard)	*fwhm*
Zn $2p_{3/2}$	1021.25	1021.2	2.47
Zn $2p_{1/2}$	1044.65	1044.3	4.79
Ag $3d_{5/2}$	368.52	368.2	2.00
Ag $3d_{3/2}$	374.51	374.1	2.26
O 1s	530.6	530.21	3.24

4. Raman studies of ZnO nanorods and hybrid ZnO@Ag core-shell nanorods:

Resonant Raman Scattering (RRS) for ZnO and hybrid ZnO@Ag (Figure S3) were carried at room temperature under 325 nm excitation wavelength, where, excitation photon energy is resonant with the electronic inter-band transition energy of the wurtzite ZnO nanorods [5]. In higher-order phonon process, the scattering intensity is large and correlated to the anion-cation bond polarity and polar character of Zn-O bonds in the nanorods [6]. In RRS spectra all the samples shows multi-phonon longitudinal optical (LO) modes upto 2nd order via the Frohlich mechanism, indicating a resonant enhancement effect of ZnO [5].

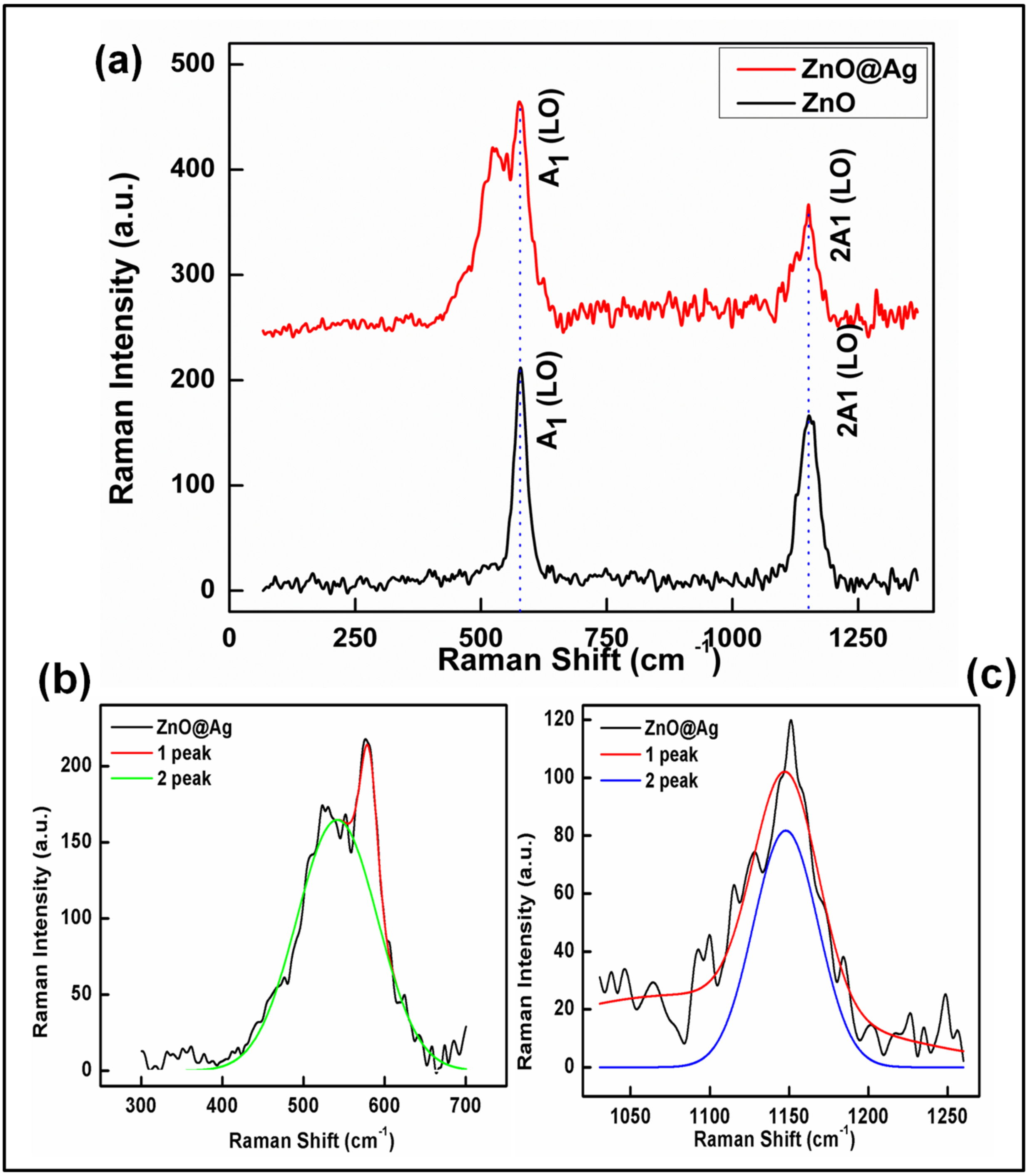

Figure S3 (a) Raman spectra of ZnO and hybrid ZnO@Ag core-shell nanorods, (b) A1 (LO) and (c) 2A1 (LO) phonon peaks of ZnO@Ag core-shell nanorods.

In general, the number of multi-phonon scattering process observed in semiconductors varies monotonically with polaron coupling coefficient. For ZnO, large number of polaron coupling coefficient till 10th order is observed [6]. Two asymmetric longitudinal optical (LO) multi-phonon peaks are observed at 579 and 1150 cm^{-1} which are attributed to the Raman A_1 (LO) phonon scattering process. The first order LO phonon of the

ZnO nanorods is centered at 579 cm^{-1} which is very close to the bulk ZnO (574 cm^{-1}) and confirms the wurtzite phase ZnO with *c* axis as growth direction [7]. According to previous reports shift in the 1-LO phonon peaks is observed, which is attributed to the optical phonon confinement, defects, tensile strain, and residual stress [8]. Resonant Raman Scattering spectra of hybrid ZnO@Ag core-shell nanorods shows a typical A_1(LO) phonon scattering at 575.8 cm^{-1}. Red shift is observed in the LO phonon, due to the polar lattice bonds between Ag-ZnO and also due to the lattice mismatch between ZnO nanorods and Ag nanoparticles [9]. Also, in ZnO@Ag spectrum the Raman peaks shows a broadening effect (Figure S3b,c) and a doublet formation which would have hoisted due to the growth of Ag nanoclusters onto the ZnO nanorods. This alteration of the lattice parameter is also confirmed from the XRD studies of hybrid ZnO@Ag core-shell nanorods. Active sites on ZnO nanorods are occupied by Ag nanoclusters on ZnO nanorods, reducing the defects in the rods and thus making the changes in the A_1 LO phonon vibrations which match with the red shift in RTPL spectra.

5. FT- IR Studies:

Formation of ZnO nanorods and hybrid ZnO@Ag core-shell nanorods was further analyzed by FT-IR spectral analysis, as shown in the Figure S4. The peaks around 3386 cm^{-1} and 1635 cm^{-1} in Figure S5a corresponding to O-H stretching vibrations of residual physisorbed water molecules on ZnO nanorods. The amino group has a characteristic absorption band in the region of 3400–3500 cm^{1}, which is masked by the broad absorption band from the –OH group. The peaks appearing at 2853 cm^{-1} and 2924 cm^{-1} correspond to symmetric and asymmetric stretching vibrations from methylene C-H group respectively. The doublet at 2360 cm^{-1} and 2335 cm^{-1} corresponds to the asymmetric stretching of adsorbed atmospheric CO_2 on the material. The bands between 1450-1500cm^{-1} are attributed to the deformation modes of -CH_2- and -CH_3 groups. CH_2 rocking vibrations appear at 889 cm^{-1}. The peak observed at 436 cm^{-1} corresponds to Zn-O stretching vibrations and confirms the presence of ZnO.

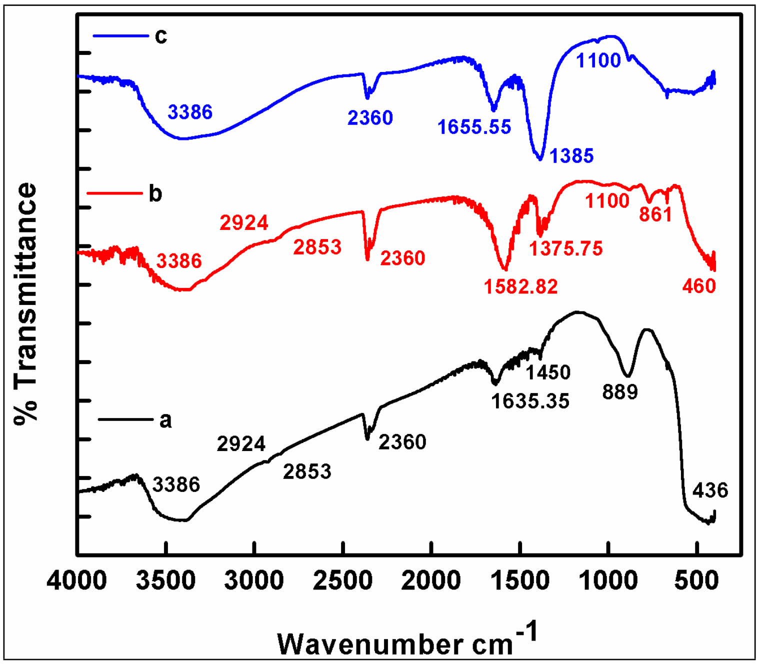

Figure. S4 FT-IR spectra of (a) ZnO nanorods, (b) APTMS functionalized ZnO nanorods and (c) hybrid ZnO@Ag core-shell nanorods.

After functionalizing with APTMS, ZnO shows additional peaks corresponding to its structure as depicted in Figure S5b confirming the functionalization process. A small signal at 1100 cm^{-1} corresponds to the characteristic Si–O–Si asymmetric stretching and peak at 861 cm^{-1} is attributed to Si–O–Si symmetric stretching. Also the Si-O-Si bending mode appears around 460 cm^{-1}. The intense peak appearing at 1582 cm^{-1} corresponds to the primary amine N-H bending vibrations of APTMS. A vibrational mode typical of aminopropyl moieties is also observed at 1375 cm^{-1} and ascribed to the wagging modes of methylene units. The characteristic features of TEA are apparent in the spectrum of the ZnO@Ag core-shell nanorods as shown in Figure S4c. The doublet appearing around 1385 cm^{-1} represents the overlapped peaks due to methylene wagging and C-N stretching from the tertiary amine group, suggesting the intervention of Triethylamine (TEA) used for the reduction process. For the hybrid ZnO@Ag core-shell nanorods, the intensity of the strong N-H bending vibration ascribed to APTMS, appearing at 1582 cm^{-1} has decreased drastically, confirming the Ag cluster shell growth on APTMS functionalized ZnO nanorod surfaces [3].

6. Thermo gravimetric analysis of ZnO nanorods and hybrid ZnO@Ag core-shell nanrods:

Thermo Gravimetric Analysis was performed for the ZnO nanorods and hybrid ZnO@Ag core-shell nanorods to study the thermal stability of materials. Figure S5 shows the TGA thermogram of the ZnO nanorods depicting the decomposition profile. ZnO nanorods show single stage decomposition with very minimum weight loss. This may be attributed to the surface dehydration and dehydroxylation. Around 98% of the materials remain stable till 600°C, proving the high thermal stability nature of ZnO nanorods. Whereas, hybrid ZnO@Ag core-shell nanorods shows three stage decomposition at 174°C, 220°C and 358°C. The thermogram shows the distinctive surface dehydration for hybrid nanomaterials at higher temperature of around 174°C, where the first weight loss occurs. The weight loss between 200°C-280°C can be ascribed to the removal of Triethylamine attached with the Ag nanoclusters. Third stage weight removal attributed to the decomposition of the linker molecules aminopropyl group at 358°C. Core-shell nanorods remain stable even at elevated temperatures; this reflects the stability of the hybrid materials and thus can be used for higher temperature applications also.

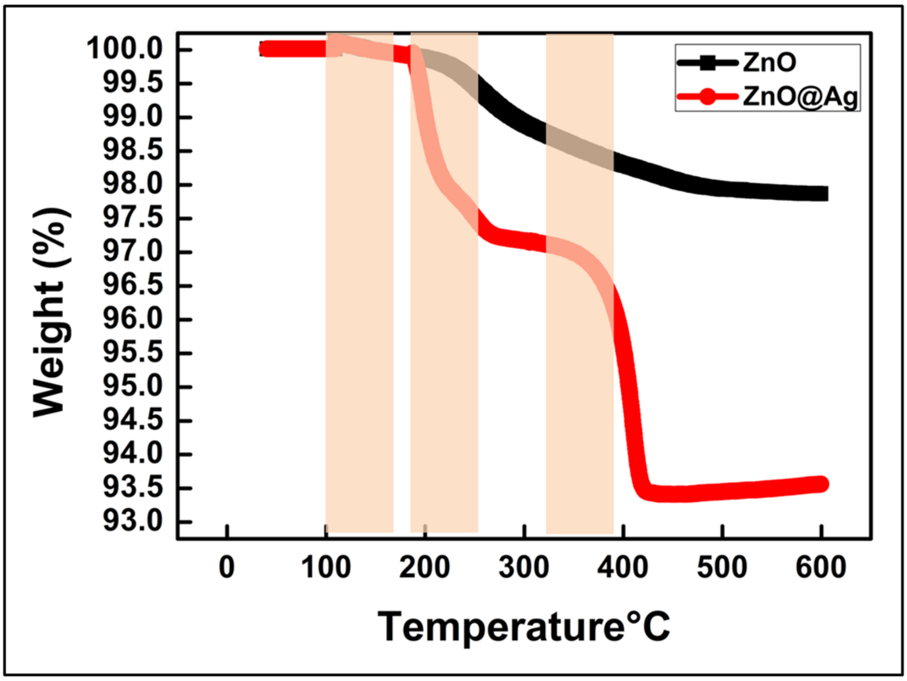

Figure S5 TGA thermograms of ZnO nanorods and hybrid ZnO@Ag core-shell nanorods.

7. Photocatalytic degradation of R6G using ZnO nanorods:

The ratio between the concentration changes of dye (C) to the relative initial concentration (C_o) during photocatalysis gives quantitative measure of the process. The corresponding C/Co degradation profiles using UV irradiation and solar irradiation are shown in Figure 8a, b respectively. From the C/C_o profile for the photodegradation of R6G, it can be proposed that degradation process follows first-order kinetics law. The first-order rate constant, k could be obtained from the expression;

$$\text{In } (C/C_o) = - kt \quad \text{---} \quad (3)$$

where, C_o is the initial concentration of dye, C is the concentration after the degradation process over time t and k is the rate constant for the reaction process.

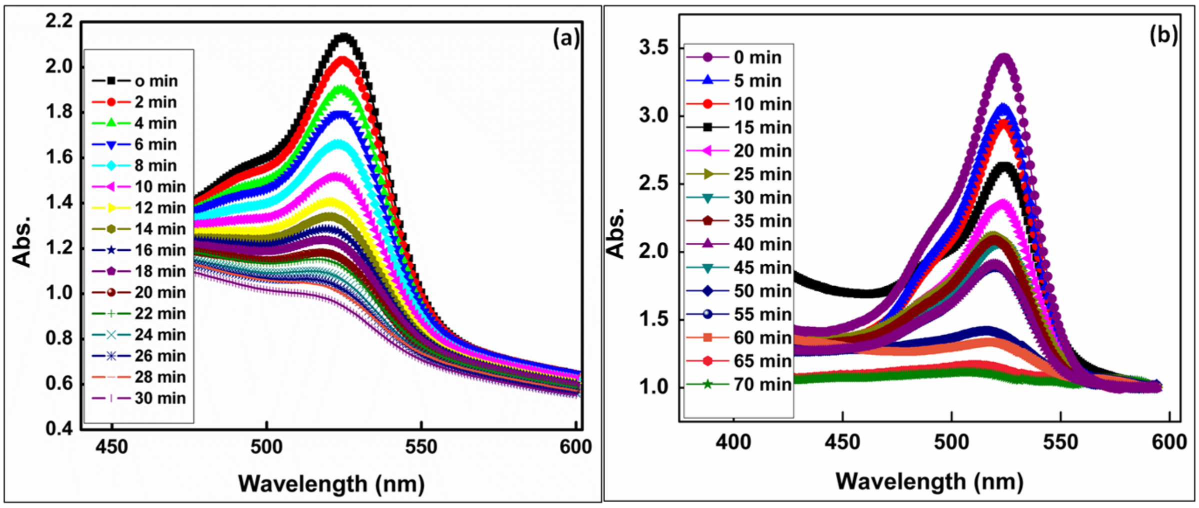

Figure S6 Optical absorbance spectra monitoring the photocatalytic degradation process of R6G dye using ZnO nanorods under (a) UV-Irradiation, and (b) Solar-Irradiation.

8. Rate constant determination:

Degradation profiles of ZnO nanorods and hybrid ZnO@Ag core-shell nanorods:

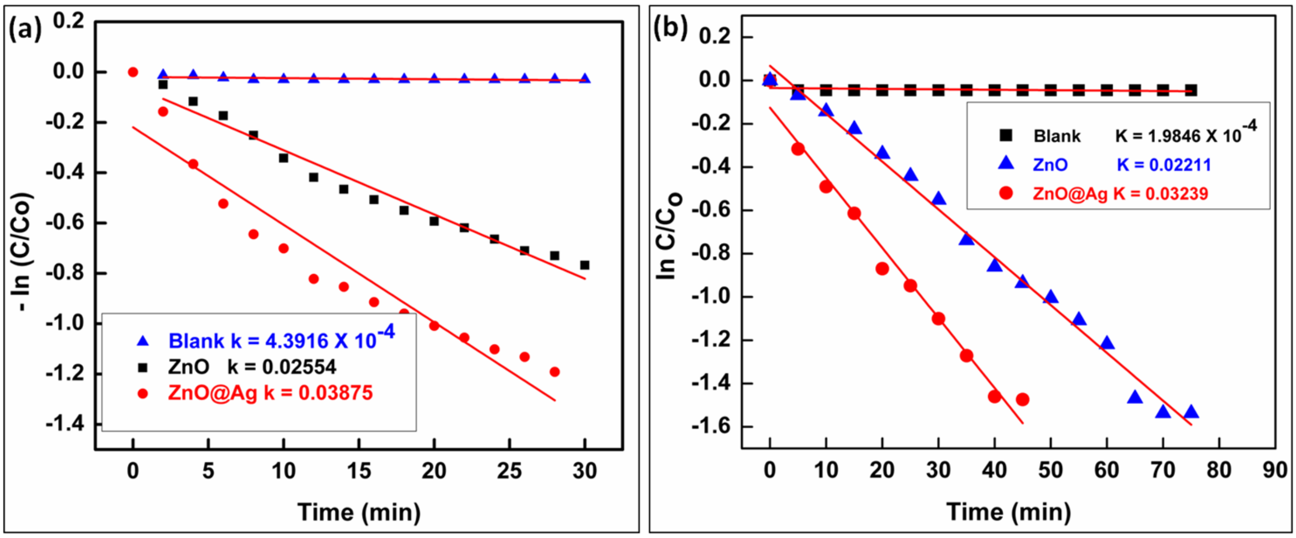

Figure S7 $In(C/C_o)$ curve as a function of time for photodegradation process of R6G dye.

9. Effect of pH:

Generally photocatalysis will be taking place at different pH as dye effluent from textile industry has a wide range of pH values. During photodegradation phenomenon generation of free radicals (OH) inside the photocatalytic solution occurs which also varies with solution pH. Thus studying the effect of pH on the photocatalysis process is significant for any photocatalytic materials. Decolourization efficiency (%) was calculated using the following equation,

$$\% \ \mathbf{Degradation} = \mathbf{C_o\text{-}C/C_o * 100}$$

Where C_o is the initial concentration of the dye, C is the concentration of dye after UV irradiation. From the Figure S7 it is noticed that for acidic pH the %degradation was found to be minimum where as for alkaline pH maximum % degradation was observed. This may be attributed to the increased hydroxyl ion production inside the solution which directly alters the reaction rate. In different pH conditions the surface properties of catalyst will be modified and dissociation of dye molecules occurs at varied reaction rate thus influencing the photocatalysis process. However, higher degradation rate is observed in alkaline pH (pH- 10).

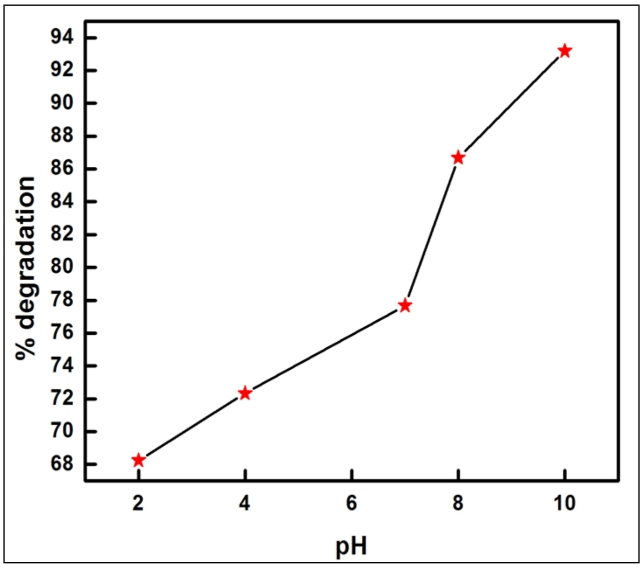

Figure S8 pH vs % degradation graph of R6G dye by ZnO@Ag core-shell nanorods.

10. Photocatalytic degradation of R6G dye using hybrid ZnO@Ag core-shell nanorods in dark condition:

Similar to the above mentioned photocatalytic degradation of R6G dye was carried out using hybrid ZnO@Ag core-shell nanorods under dark condition. Dark environment was maintained throughout the studies and its corresponding UV-visible spectroscopy measurements are shown in Figure S9. No major changes were observed for the characteristic peak monitored at 525 nm for 30 minutes. It clearly emphasis the degradation phenomenon was photo-dependent process.

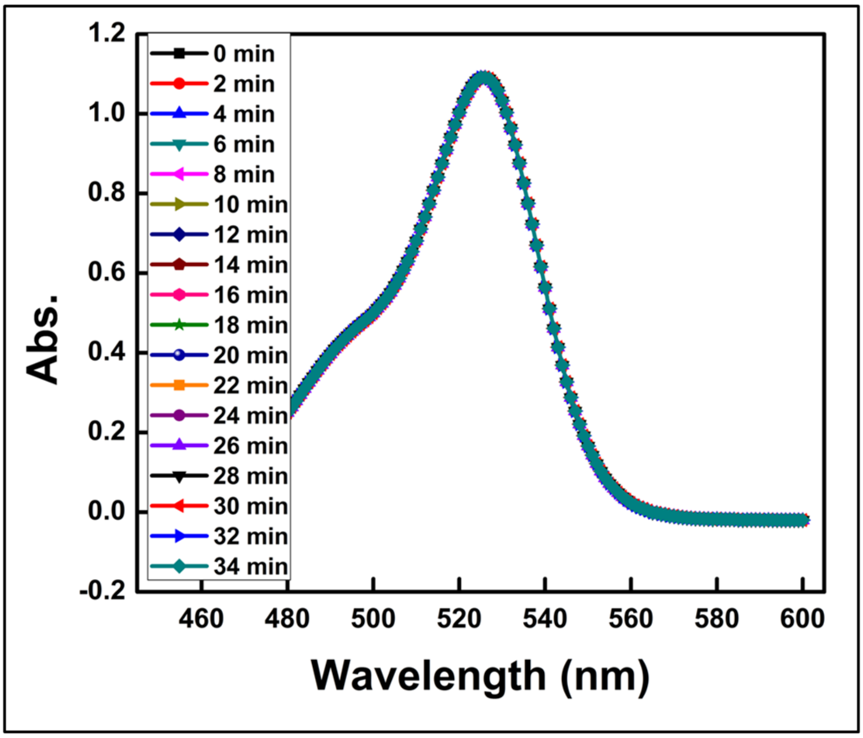

Figure S9 Optical absorbance spectra monitoring the photocatalytic degradation process of R6G dye using hybrid ZnO@Ag core0shell nanorods under dark condition

11. Photocatalytic degradation of Congo red using ZnO nanorods:

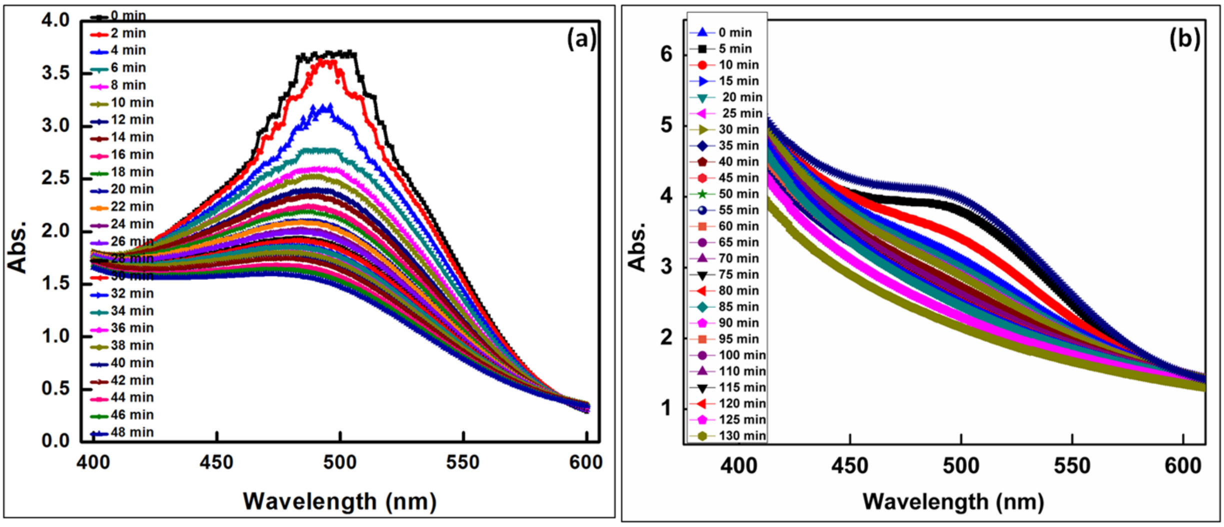

Figure S10 Optical absorbance spectra monitoring the photocatalytic degradation process of Congo red dyes using ZnO nanorods under (a) UV-Irradiation, and (b) Solar-Irradiation.

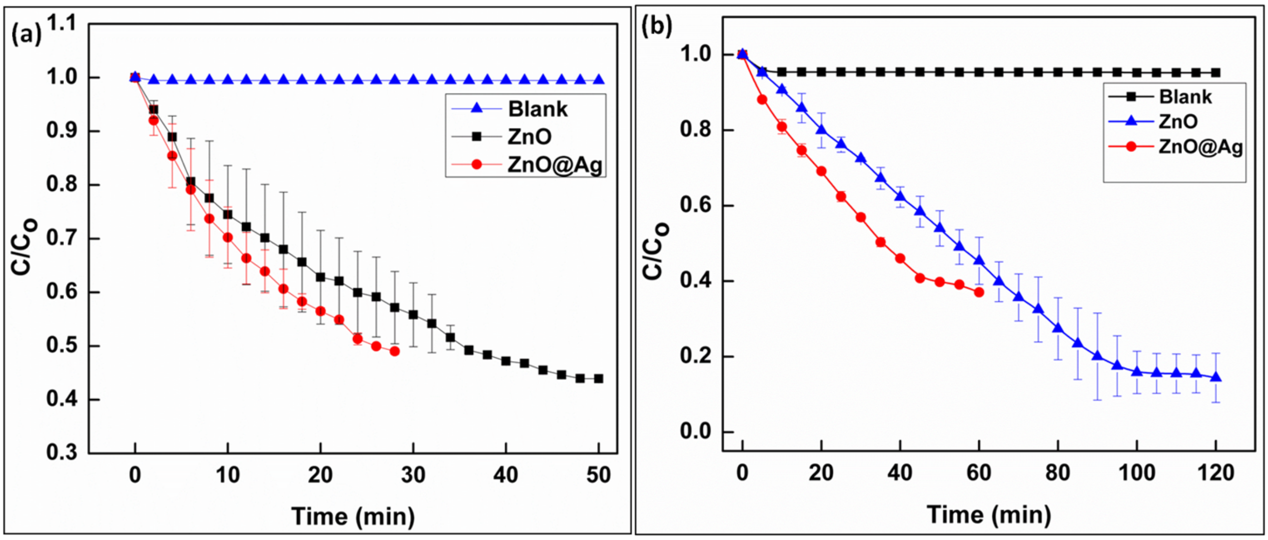

Figure S11 C/C_o graph for the photocatalytic degradation of Congo Red under (a) UV irradiation and (b) solar irradiation.

12. Photocatalytic degradation of Amido Black using ZnO nanorods:

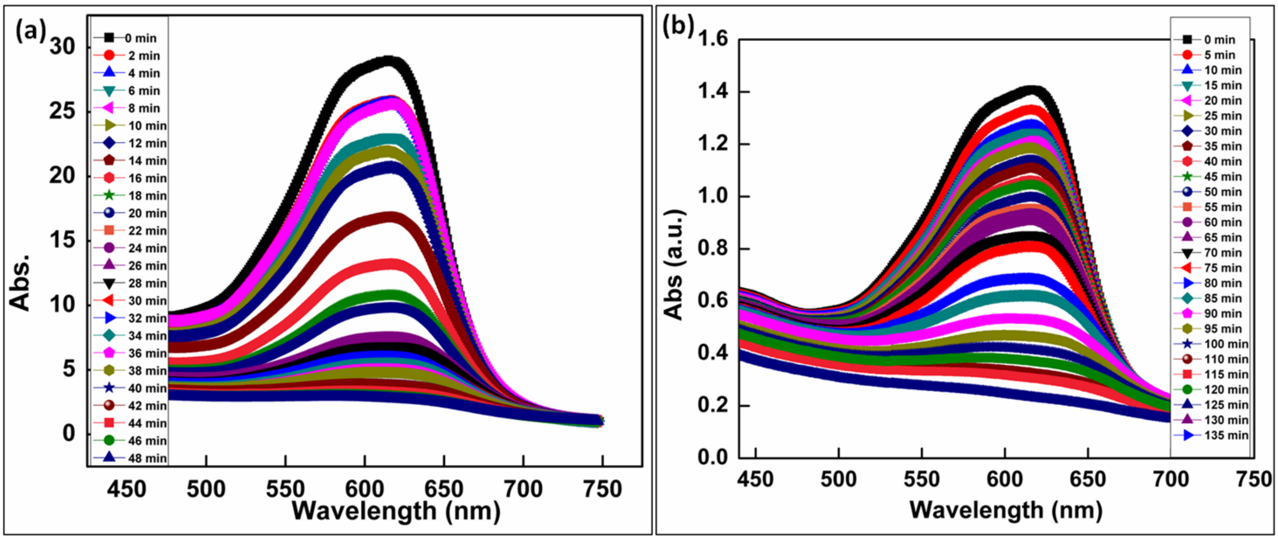

Figure S12 Optical absorbance spectra monitoring the photocatalytic degradation process of Amido Black dyes using ZnO nanorods under (a) UV-irradiation, and (b) Solar-irradiation.

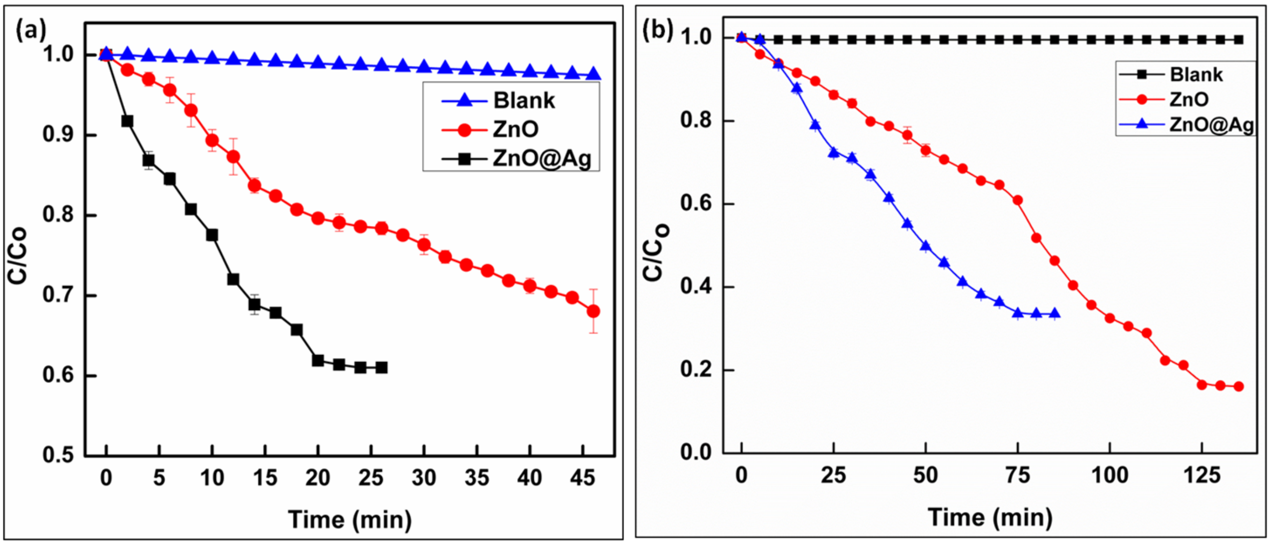

Figure S13 *C/C_o* graph for the photocatalytic degradation of Amido black 10B under (a) UV-Irradiation and (b) Solar-Irradiation.

13. Photocatalytic degradation of Textile effluent using ZnO nanorods:

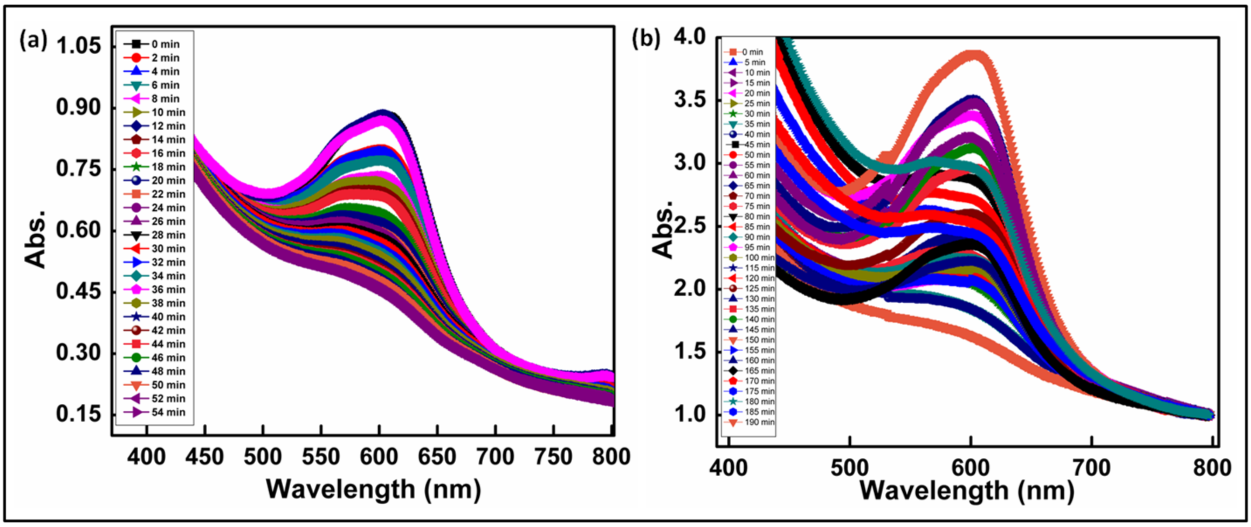

Figure S14 Optical absorbance spectra monitoring the photocatalytic degradation process of Textile effluent using ZnO nanorods under (a) UV-irradiation, and (b) Solar-irradiation.

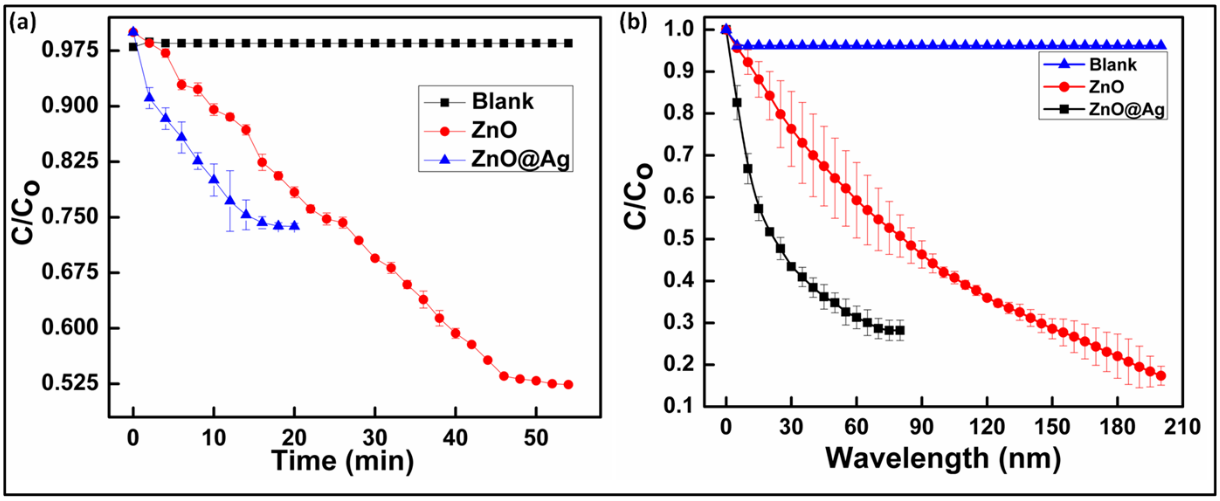

Figure S15 *C/C_o* graph for the photocatalytic degradation of Textile effluent under (a) UV-Irradiation and (b) Solar-Irradiation.

Table S3. Comparison of rate constant (*k*) for R6G, Congo red and Amido Black dyes using ZnO nanorods and hybrid ZnO@Ag core-shell nanorods.

Sample	Rate constant *k* (min $^{-1}$) for R6G dye		Rate constant *k* (min $^{-1}$) Congo red		Rate constant *k* (min $^{-1}$) Amido Black	
	UV irradiation	Solar irradiation	UV irradiation	Solar irradiation	UV irradiation	Solar irradiation
Blank	4.346×10^{-4}	1.983×10^{-4}	8.23×10^{-5}	1.06×10^{-4}	8.33×10^{-5}	6.08×10^{-6}
ZnO-NR	0.02554	0.02211	0.01542	0.01559	0.0078	0.01387
ZnO@Ag	0.03875	0.03239	0.02487	0.01867	0.01943	0.01474

References:

1. K. A. Alim, V. A. Fonoberov, M. Shamsa and A. A. Balandin, *J. Appl. Phys., 2005*, 97, 124313.
2. W. Xin, K. Xianggui, Y. Yi and Z. Hong, *J. Phys. Chem. C., 2007*, 111, 3836-3841.
3. American Society for Testing and Material. Powder Diffraction Files; Joint Committee on Powder Diffraction Standards: Swarthmore, PA, 1999, pp 3-888.
4. X. Wang, J. Song,J. Liu, J and Z.L. Wang, *Science, 2007*, 316, 102-105.
5. H.S. Kang, B. D. Ahn, J. H. Kim, G.H. Kim, S. H. Lim, H. W. Chang, and S. Y. Lee, *Appl. Phys. Lett., 2006*, 88, 202108.
6. Y. Zhang, N. Kohler and M. Zhang, *Biomaterials, 2002*, 23, 1553–1561.
7. B. Kumar, H. Gong, S. Y. Chow, S. Tripathy and Y. N. Hua, *Appl. Phys. Lett., 2006*, 89, 071922-071924.
8. U. Ozgur, Y. I. Alivov, C. Liu, A. Teke, M. A. Reshchikov, S. Dogan, V. Avrutin, S. J. Cho and H. A. Morkoc, *J. Appl. Phys., 2005*, 98, 041301-041303.